Phosphoinositide-dependent enrichment of actin monomers in dendritic spines regulates synapse development and plasticity

Wenliang Lei,[1,3] Kenneth R. Myers,[1,3] Yanfang Rui,[1,3] Siarhei Hladyshau,[4] Denis Tsygankov,[4] and James Q. Zheng[1,2,3]

[1]Department of Cell Biology, [2]Department of Neurology, and [3]Center for Neurodegenerative Diseases, Emory University School of Medicine, Atlanta, GA
[4]Wallace H. Coulter Department of Biomedical Engineering, Georgia Institute of Technology and Emory University, Atlanta, GA

Dendritic spines are small postsynaptic compartments of excitatory synapses in the vertebrate brain that are modified during learning, aging, and neurological disorders. The formation and modification of dendritic spines depend on rapid assembly and dynamic remodeling of the actin cytoskeleton in this highly compartmentalized space, but the precise mechanisms remain to be fully elucidated. In this study, we report that spatiotemporal enrichment of actin monomers (G-actin) in dendritic spines regulates spine development and plasticity. We first show that dendritic spines contain a locally enriched pool of G-actin that can be regulated by synaptic activity. We further find that this G-actin pool functions in spine development and its modification during synaptic plasticity. Mechanistically, the relatively immobile G-actin pool in spines depends on the phosphoinositide PI(3,4,5)P_3 and involves the actin monomer–binding protein profilin. Together, our results have revealed a novel mechanism by which dynamic enrichment of G-actin in spines regulates the actin remodeling underlying synapse development and plasticity.

Introduction

Dendritic spines are small membranous protrusions on neurons that serve as the postsynaptic platform for most of the excitatory synapses in the vertebrate brain (Nimchinsky et al., 2002). Spines undergo short- and long-term structural modifications during the developmental refinement of neural circuits, as well as during learning and memory (Geinisman, 2000; Yuste and Bonhoeffer, 2001; Halpain et al., 2005; Segal, 2005). Spine formation and morphology are altered in response to extracellular stimuli, such as synaptic activity. For example, in models of learning and memory such as hippocampal long-term potentiation (LTP), the enlargement of existing spine heads, emergence of new spines, and shortening of spine necks have been observed (Yuste and Bonhoeffer, 2001). These changes have been proposed to consolidate synaptic modifications (Segal, 2005). Because dendritic spines are crucial for normal synaptic transmission, defects in or the loss of spines have been strongly associated with numerous neural disorders (Penzes et al., 2011). Therefore, a better understanding of the molecular and cellular mechanisms underlying synaptic development and plasticity is essential to our understanding of brain development and how it is altered in neurological diseases.

The actin cytoskeleton is the primary driver of spine structure and modification (Hotulainen and Hoogenraad, 2010), although the precise mechanisms regulating its assembly remain to be fully elucidated. The filamentous actin (F-actin) structures in cells are built from globular actin monomers (G-actin) under complex regulation by accessory proteins (Pollard et al., 2000). Individual filaments are assembled through polymerization of G-actin occurring at the barbed end and the depolymerization of F-actin at the pointed end. A wide range of accessory proteins regulate the assembly and disassembly rate, as well as organize the filaments into distinct complex networks for different cellular functions (Pollard and Borisy, 2003; Chhabra and Higgs, 2007). G-actin is generally thought to exist as a single diffusible reservoir in the cell to passively support actin dynamics. However, we have recently shown that a pool of G-actin is dynamically concentrated at the leading edge of protruding lamellipodia of motile cells and nerve growth cones to promote F-actin polymerization and membrane protrusion (Lee et al., 2013). These findings suggest that spatiotemporal targeting of G-actin could represent an important mechanism for local control and regulation of actin assembly and remodeling. By dynamically controlling the local concentration and nucleotide status of actin monomers, one could directly regulate actin assembly and disassembly underlying spatiotemporally restricted cellular activities.

The development of mature dendritic spines depends on the polymerization of G-actin into distinct F-actin networks

Correspondence to James Q. Zheng: james.zheng@emory.edu

Abbreviations used: DBP, vitamin D–binding protein; DIV, days in vitro; FRAP, fluorescence recovery after photobleaching; LTP, long-term potentiation; PH, pleckstrin homology; PTEN, phosphatase and tensin homologue; SHP, spine head protrusion; TEA, tetraethylammonium.

The Rockefeller University Press
J. Cell Biol. Vol. 216 No. 8 2551–2564
https://doi.org/10.1083/jcb.201612042

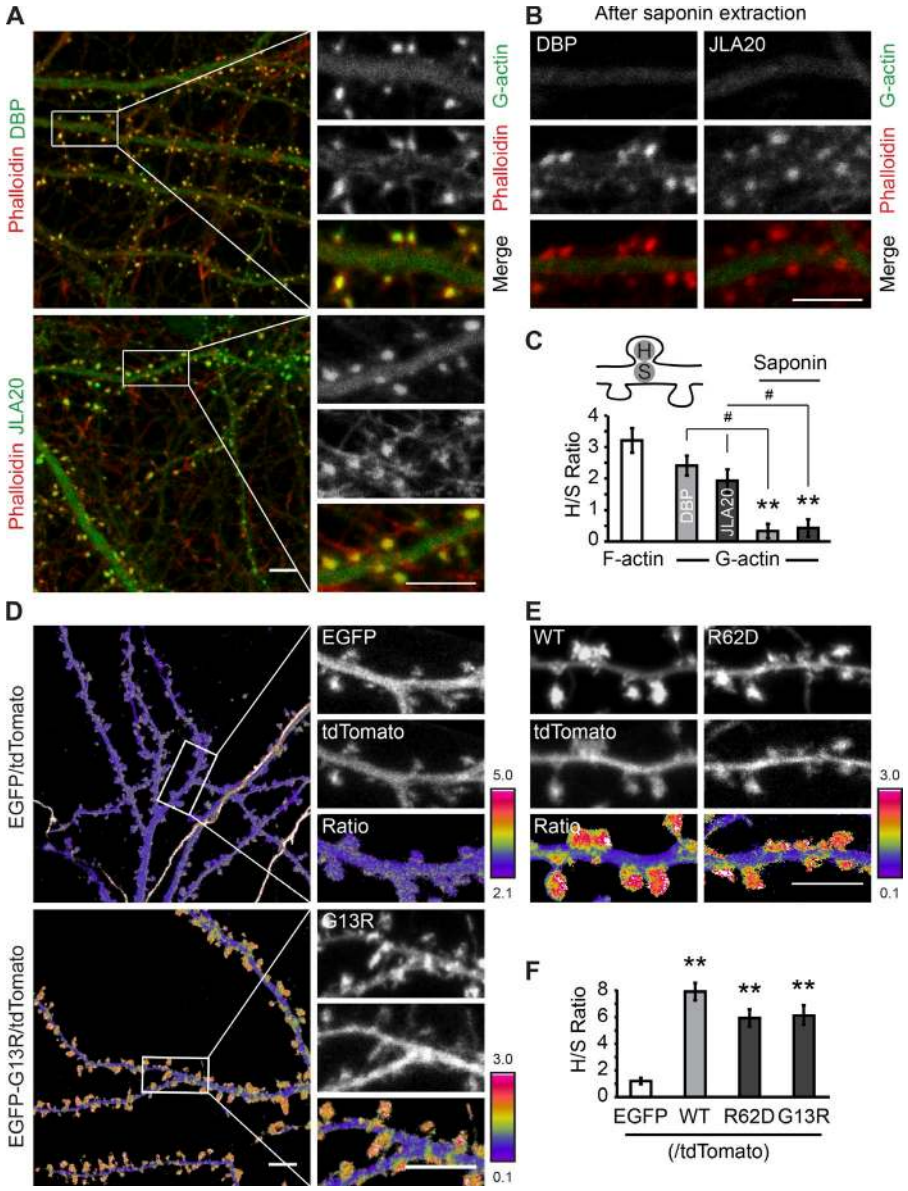

Figure 1. **Spine enrichment of actin monomers (G-actin) in cultured hippocampal neurons.** (A) Representative images showing the enrichment of G-actin in spines as revealed by specific G-actin probes DBP and JLA20. Spines are highlighted by Alexa Fluor 569 phalloidin. Bars, 5 µm. (B) Representative images showing that live-cell extraction by saponin removed the G-actin signals in spines. Bar, 5 µm. (C) Quantification of the spine enrichment of G-actin by normalizing the spine signals to the adjacent shaft signals. Error bars represent the SEM. $P < 0.01$; one-way ANOVA. Tukey's posthoc test: **, $P < 0.01$; G-actin saponin treatment group versus F-actin group; #, $P < 0.05$; G-actin saponin treatment group versus G-actin no treatment group. (D and E) Representative images showing the enrichment of G-actin in spines by live-cell imaging. Rat hippocampal neurons expressing EGFP, EGFP-WT actin, EGFP-R62D, and EGFPG13R actin mutants are shown. The cells expressed tdTomato as a volume marker, and ratiometric images are shown to highlight the spine enrichment of G-actin. Bars, 5 µm. (F) Quantification of spine enrichment of G-actin from the live-imaging data. Similarly, spine signals were normalized against the adjacent shaft signals. Error bars represent the SEM. $P < 0.01$; one-way ANOVA. Tukey's posthoc test: **, $P < 0.01$; EGFP group versus WT, R62D, or G13R group. (C and F) Results were averaged from 40 spines from three batches of culture, and the data distribution was tested for normality with the Shapiro-Wilk test. H/S, spine head to shaft.

(Hotulainen and Hoogenraad, 2010; Korobova and Svitkina, 2010). Dendritic spines contain a small bulbous head followed by a neck that has been shown to limit diffusion with the adjacent dendritic shaft (Bloodgood and Sabatini, 2005). As such, an increase in F-actin for spine enlargement during development and synaptic potentiation requires the availability of a sufficient amount of G-actin that can be rapidly incorporated into the F-actin networks. In this study, we have provided evidence for the first time that G-actin is locally enriched in dendritic spines. Importantly, the enrichment of G-actin in spines can be regulated by synaptic activity and plays a crucial role in both spine development and plasticity. Through a combination of experimental analysis and computational modeling, we have shown that G-actin is preferentially enriched in spines through an association with phosphoinositides. We further demonstrate a role for the actin monomer–binding protein profilin in G-actin spine enrichment. Thus, our work has uncovered an exciting mechanism by which the spatiotemporal regulation of local G-actin in spines by synaptic activity regulates actin assembly and spine remodeling.

Results

We fluorescently stained G-actin using two probes that we have previously verified to be specific for actin monomers: vitamin D–binding protein (DBP) and JLA20 anti-actin antibody (Lee et al., 2013). Hippocampal neurons cultured for 21 d in vitro (DIV21) exhibited numerous spines on dendritic processes, as highlighted by a low dose of fluorescent phalloidin (Gu et al., 2008), of which many displayed a mushroom morphology (Fig. 1 A). Strikingly, both DBP and JLA20 highlighted the spines with strong signals, indicating that G-actin is enriched in dendritic spines (Fig. 1 A). The G-actin signals appear to be mostly concentrated in the spine head, not in the spine neck where F-actin is also abundant (see the enlarged color panels in Fig. 1 A). Importantly, live-cell extraction using the mild detergent saponin completely removed DBP or JLA20 signals in spines without affecting the F-actin signals labeled by fluorescent phalloidin (Fig. 1 B), confirming the specificity of both probes for G-actin. Quantitative measurements show that the G-actin signals (labeled by either DBP or JLA20) are over

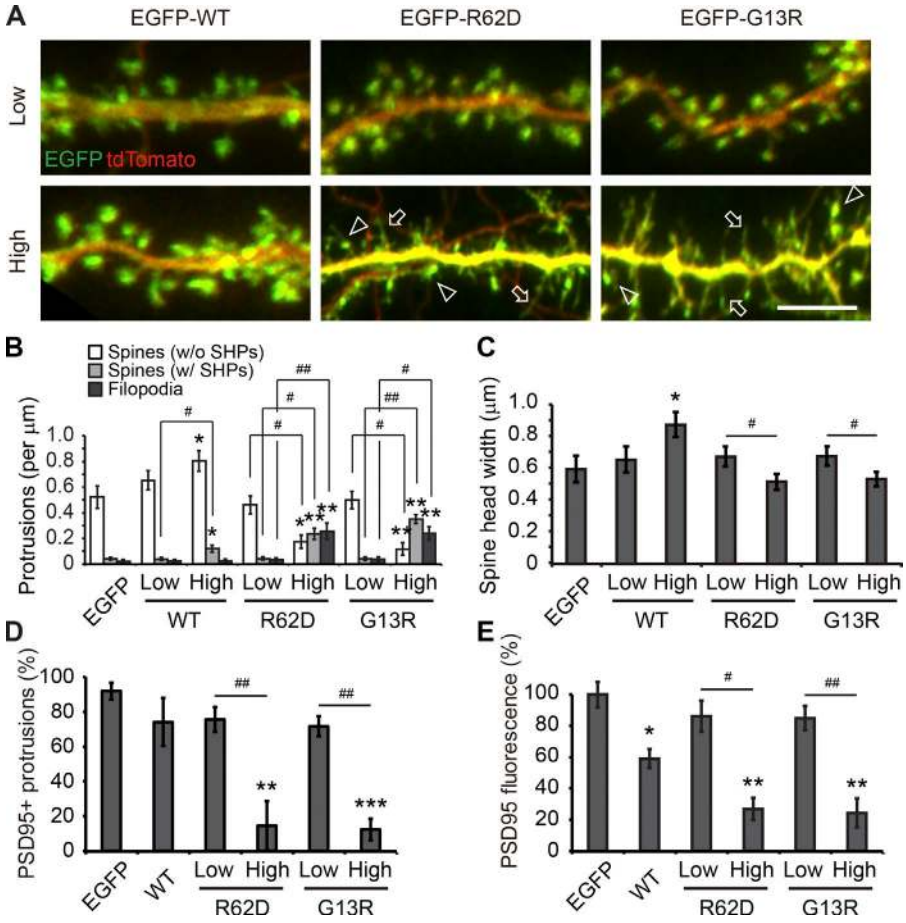

Figure 2. **Expression of EGFP-tagged actin and actin mutants affects spine development and synapse formation.** (A) Representative images showing hippocampal neurons expressing low and high levels of EGFP-tagged actin proteins. Relatively high-expression levels of EGFP-G13R and EGFP-R62D caused reductions in the number of mushroom-shaped spines and increases in the number of deformed spines with both SHPs and filopodia-like protrusions. Arrows indicate filopodia, and arrowheads point to deformed spines with SHPs. Bar, 5 µm. (B) Quantification of different dendritic protrusions. $P < 0.001$; two-way ANOVA. Tukey's posthoc test: *, $P < 0.05$; **, $P < 0.01$; EGFP group versus WT, R62D, or G13R high-expression group; #, $P < 0.05$; ##, $P < 0.01$; WT, R62D, or G13R low-expression group versus WT, R62D, or G13R high-expression group. w/, with; w/o, without. (C) Quantification of spine head width of neurons expressing different levels of EGFP, EGFP-WT, EGFP-G13R, and EGFP-R62D. $P < 0.01$; one-way ANOVA. Tukey's posthoc test: *, $P < 0.05$; EGFP group versus WT high-expression group; #, $P < 0.05$; R62D or G13R low-expression group versus R62D or G13R high-expression group. (B and C) Results were averaged from 50 spines from three batches of culture, and the data distribution was tested for normality with the Shapiro-Wilk test. (D and E) Quantification of the number of protrusions containing PSD95 and the size of PSD95 in dendritic protrusions of neurons expressing different levels of EGFP, EGFP-WT, EGFP-G13R, and EGFP-R62D. $P < 0.001$ (D) or $P < 0.01$ (E); one-way ANOVA. Tukey's posthoc test: *, $P < 0.05$; **, $P < 0.01$; ***, $P < 0.001$; EGFP group versus WT, R62D high-expression, or G13R high-expression group; #, $P < 0.05$; ##, $P < 0.01$; R62D or G13R low-expression group versus R62D or G13R high-expression group. Results were averaged from 30 spines from three batches of culture, and the data distribution was tested for normality with the Shapiro-Wilk test. Error bars represent the SEM.

twice as high in the spine head as in the adjacent dendritic shaft region and, importantly, can be effectively removed by saponin (Fig. 1 C). Therefore, dendritic spines contain a concentrated pool of G-actin.

The enrichment of G-actin in spines was further confirmed by live-cell imaging of two EGFP-tagged nonpolymerizable γ-actin mutants, G13R and R62D (Posern et al., 2002). To control for the volume, we coexpressed soluble tdTomato and visualized the actin distribution using the ratio of EGFP to tdTomato. As expected, the ratiometric distribution of soluble EGFP was uniform throughout the cell, whereas EGFP-G13R and EGFP-R62D exhibited an enriched pattern in dendritic spines similar to that of EGFP-tagged WT (EGFP-WT) γ-actin (Fig. 1, D and E). The spine head-to-shaft ratio shows that both actin mutants are similarly enriched in spines (Fig. 1 F). Live-cell extraction by saponin also led to the loss of both actin mutants from spines, whereas a substantial amount of EGFP-WT actin signals remained (Fig. S1, A and B), confirming that these two mutants did not get incorporated into F-actin. Furthermore, the G-actin signals in spines were found to positively correlate with postsynaptic size as measured by either the spine F-actin or PSD95 signals, suggesting that G-actin is similarly concentrated in spines of different sizes (Fig. S1, C–F). Finally, the spine enrichment of G-actin was also observed in pyramidal neurons of organotypic hippocampal slices, suggesting that it represents an important postsynaptic feature in vivo (Fig. S2). Together, these results indicate the presence of a bona fide pool of G-actin enriched specifically in postsynaptic spines.

The presence of a pool of G-actin in spines suggests that it may function in actin polymerization underlying spine development. This notion is supported by the findings that hippocampal neurons expressing a high level of either EGFP-G13R or EGFP-R62D exhibited a reduced number of mushroom-shaped spines, an increased number of filopodia, and the appearance of deformed spines with spine head protrusions (SHPs), whereas the low-level expression of these actin mutants had only minimal effects (Fig. 2 A). Based on the quantification of the total level of actin proteins using immunostaining, the high- and low-expressing groups of cells are estimated to have expressed the exogenous GFP-actin at ~87 and ~14% of the endogenous actin level, respectively (Fig. S3, A and B). Our quantification of dendritic protrusion number and morphology confirmed the reduction in mushroom-shaped spines and the increase in filopodia and spines with SHPs only when the actin mutants were expressed at high levels (Fig. 2 B). Importantly, the total number of dendritic protrusions was not altered by these two actin mutants

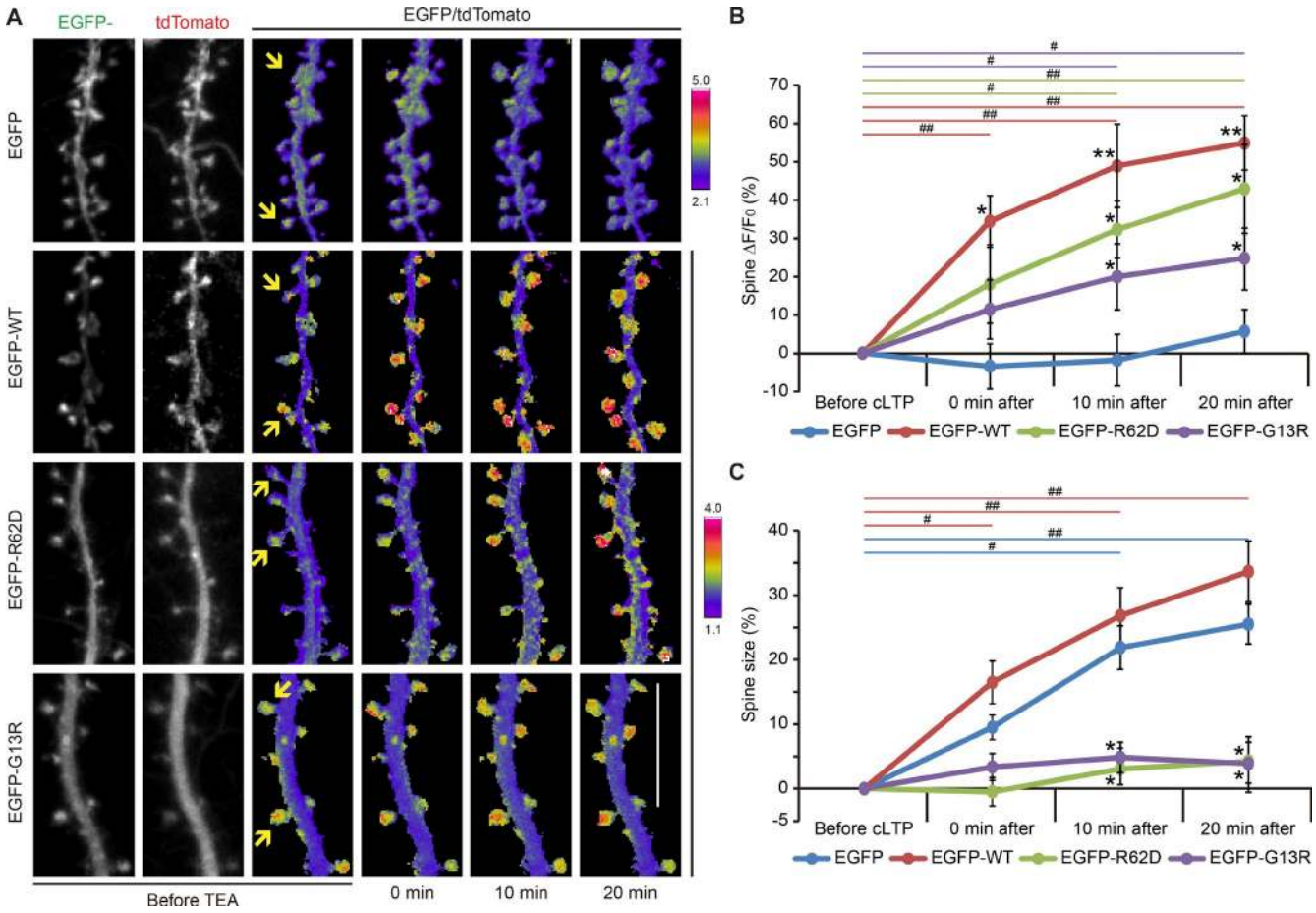

Figure 3. **Activity-dependent G-actin enrichment in dendritic spines during synaptic potentiation.** (A) Representative images showing the spine enrichment of EGFP-WT actin, EGFP-R62D, and EGFP-G13R after chemical LTP induction. The yellow arrows indicate representative spines exhibiting an increase in fluorescence with (EGFP and EGFP-WT) and without (R62 and G13R) spine enlargement. Bar, 5 µm. (B) Quantification of the EGFP fluorescence in spines at various times before and after cLTP induction. $P < 0.001$; two-way repeated-measures ANOVA over time. Bonferroni posthoc test: #, $P < 0.05$; ##, $P < 0.01$; WT, R62D, or G13R group compared with pre-LTP baseline level; *, $P < 0.05$; **, $P < 0.01$; WT, R62D, or G13R group versus EGFP group. (C) Quantification of the spine-size change at various times before and after cLTP induction. $P < 0.001$; two-way repeated measures ANOVA over time. Bonferroni posthoc test: #, $P < 0.05$; ##, $P < 0.01$; EGFP or WT group compared with pre-LTP baseline level; *, $P < 0.05$; R62D or G13R group versus EGFP group. (B and C) Results were averaged from 20 spines from three batches of culture, and the data distribution was tested for normality with the Shapiro-Wilk test. Error bars represent the SEM.

(Fig. S3 C). The spine head width, but not the spine neck length, of cells overexpressing EGFP-G13R or EGFP-R62D was also reduced in comparison with the EGFP-WT–expressing group (Fig. 2 C and Fig. S3 D). Similar to the results reported previously (Johnson and Ouimet, 2006), overexpression of EGFP-WT enhanced the development of mushroom-shaped spines (Fig. 2, B and C) and increased the total number of dendritic protrusions (Fig. S3 C). Finally, we found that expression of EGFP-R62D and EGFP-G13R at high levels markedly reduced the synapse number as assessed by PSD95 signals (Fig. 2, D and E; and Fig. S3 E). It is plausible that the nonpolymerizable actin mutants, when expressed at high levels, might have acted as dominant-negatives to disrupt normal F-actin assembly throughout the cell. However, two pieces of data argue against this possibility. First, as presented above, the total number of dendritic protrusions was not affected by these two actin mutants. Second, the overall dendritic arbor formation was not altered by overexpressing these two actin mutants (Fig. S3, F and G). Therefore, we hypothesize that it is the local enrichment of these actin mutants in spines that may enable them to compete with the endogenous actin monomers to retard the actin assembly underlying spine formation.

We next examined whether the spine enrichment of G-actin undergoes activity-dependent changes and plays a role in spine enlargement during synaptic LTP. We used a chemical LTP approach in which the potassium channel blocker tetraethylammonium (TEA) was briefly applied (10 min; hereafter referred to as TEA-cLTP) to robustly potentiate excitatory synaptic transmission and spine size (Gu et al., 2010). Live imaging of cells coexpressing EGFP-tagged actin mutants and tdTomato was performed to monitor the changes in spine size and actin enrichment. To prevent any complications caused by preexisting defects in spine morphology or density, we specifically chose neurons expressing low levels of EGFP-actin or actin mutants. Our control hippocampal neurons expressing EGFP exhibited a substantial increase in spine size after TEA-cLTP, but the EGFP/tdTomato ratio remained constant throughout the neuron (Fig. 3). However, the fluorescence of EGFP-WT and its ratio against tdTomato in spines substantially increased after TEA-cLTP, coinciding with spine enlargement (Fig. 3).

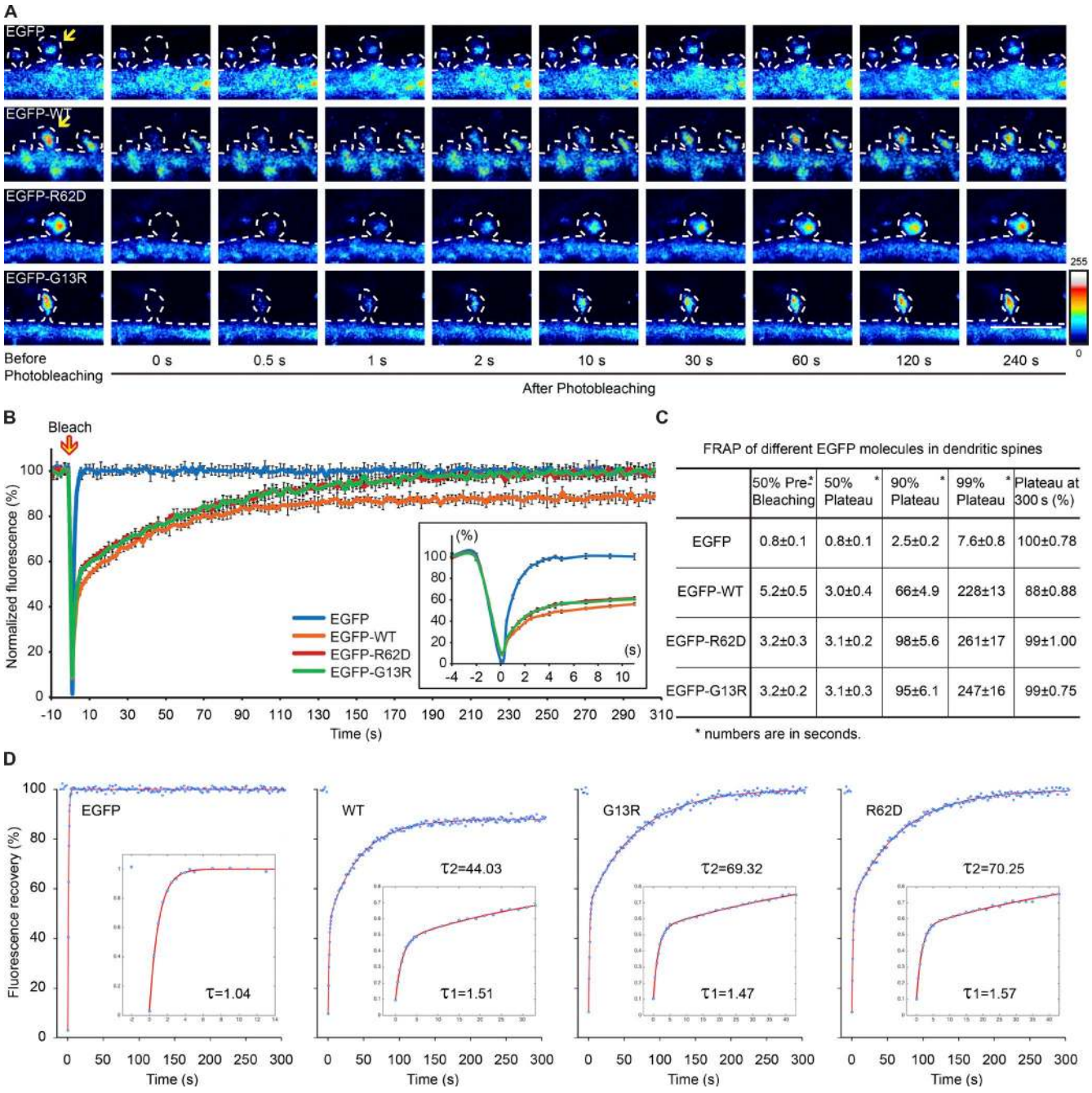

	50% Pre-Bleaching*	50% Plateau*	90% Plateau*	99% Plateau*	Plateau at 300 s (%)
EGFP	0.8±0.1	0.8±0.1	2.5±0.2	7.6±0.8	100±0.78
EGFP-WT	5.2±0.5	3.0±0.4	66±4.9	228±13	88±0.88
EGFP-R62D	3.2±0.3	3.1±0.2	98±5.6	261±17	99±1.00
EGFP-G13R	3.2±0.2	3.1±0.3	95±6.1	247±16	99±0.75

* numbers are in seconds.

Figure 4. **FRAP analysis of the G-actin pool enriched in spines.** (A) Representative image sequences showing the fluorescence recovery of EGFP, EGFP-WT actin, EGFP-R62D, and EGFP-G13R after single-spine photobleaching. The dashed lines outline the dendritic segment and spines, and the yellow arrows indicate the specific spines subjected to photobleaching when several spines are present. Bar, 5 µm. (B) FRAP curves for different EGFP proteins. The fluorescent signals in spines are normalized to the prebleaching mean and corrected for the imaging-caused bleaching using the signals from the adjacent shaft regions. $n = 6$ for each group, and error bars represent the SEM. (C) Quantification table showing recovery time for 50% prebleaching levels, 50% plateau levels, 90% and 99% plateau levels, and the final recovery percentages of different EGFP molecules in dendritic spines. All numbers are presented as mean ± SEM. (D) Curve fitting for the FRAP data. The EGFP FRAP data can be fitted with a single exponential curve, whereas the actin FRAP data (WT, G13R, and R62D) can only be fitted accurately with double exponential functions. For each FRAP group, six spines from six different neurons were examined and quantified.

Interestingly, we found that the levels of both EGFP-G13R and EGFP-R62D also increased in spines after TEA-cLTP, as indicated by their elevated ratio against tdTomato (Fig. 3). Importantly, cells expressing EGFP-G13R or EGFP-R62D showed no spine enlargement after TEA-cLTP even though both mutants were expressed at a low level that did not affect normal spine development (Fig. 3). Similar results were obtained in hippocampal neurons using glutamate-induced chemical LTP (Fig. S4). These data suggest that spine enrichment of G-actin (a) may represent the first step leading to actin polymerization underlying spine enlargement, (b) does not depend on actin polymerization, and (c) can be regulated by synaptic activity.

To elucidate the potential mechanisms underlying the spine enrichment of G-actin, we performed a fluorescence re-

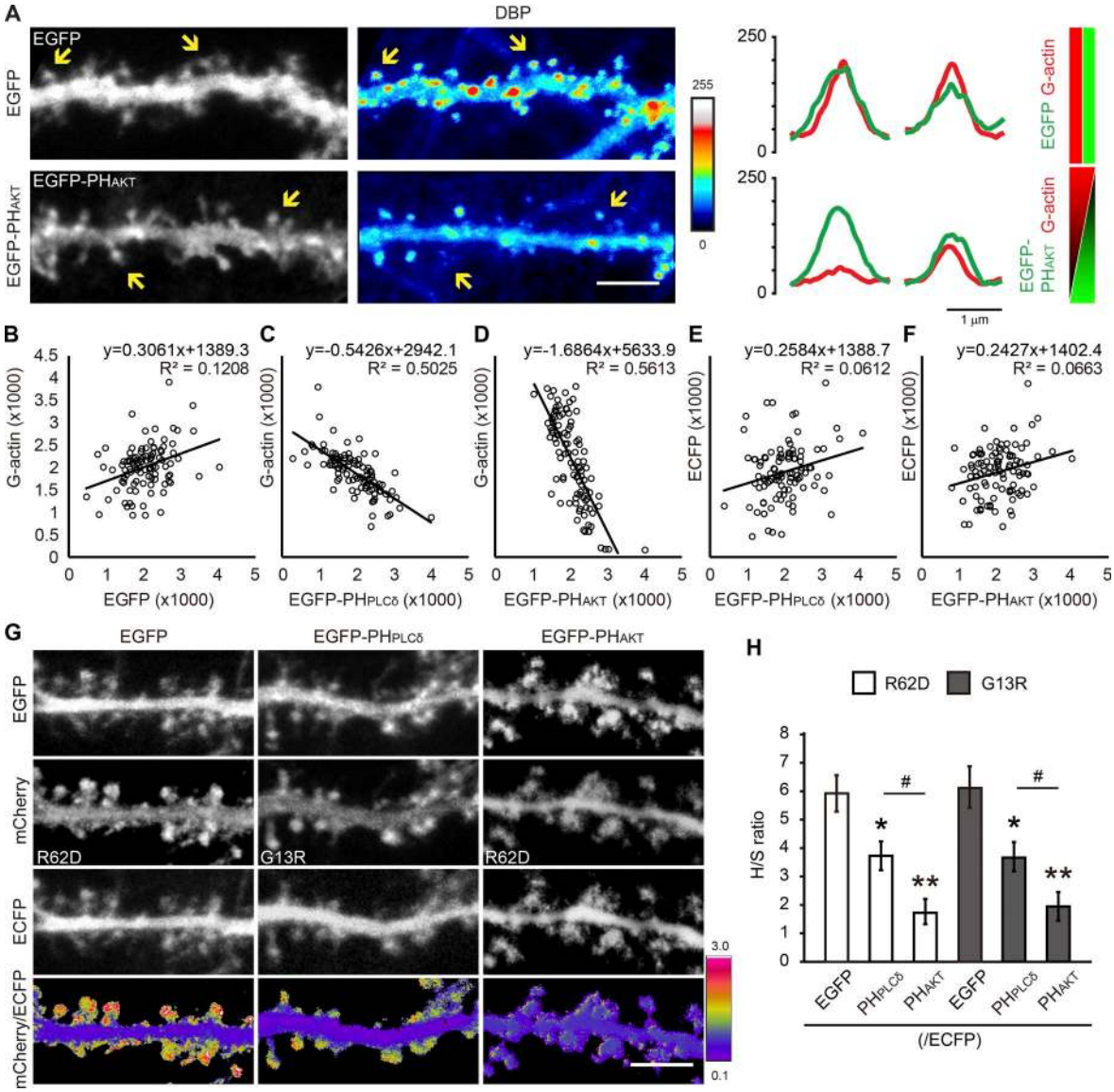

Figure 5. **Phosphoinositides mediate the spine enrichment of G-actin.** (A) Representative images and fluorescence profiles showing the effects of EGFP-tagged PH domain expression on endogenous G-actin in spines. The yellow arrows mark representative spines. Bar, 5 µm. (B–F) Correlation plots of the gray levels (12 bit) of EGFP-PH domain fluorescence and G-actin signals in spines. R^2 values were extracted from linear regression models. (G) Representative images of live cells showing the effects of EGFP-tagged PH domain expression on G-actin enrichment in spines. mCherry/ECFP ratiometric images are shown to highlight G-actin levels in spines. Bar, 5 µm. H/S, spine head to shaft. (H) Quantification of the G-actin levels in spines from the live-imaging data. Error bars represent the SEM. $P < 0.01$; two-way ANOVA. Tukey's posthoc test: *, $P < 0.05$; **, $P < 0.01$; EGFP group versus $PH_{PLC\delta}$ or PH_{AKT} group; #, $P < 0.05$; $PH_{PLC\delta}$ group versus PH_{AKT} group. Results were averaged from 30 spines from three batches of culture, and the data distribution was tested for normality with the Shapiro-Wilk test.

covery after photobleaching (FRAP) assay to examine the mobility of G-actin in individual spines (Fig. 4). As expected, EGFP fluorescence in spines recovered rapidly after photobleaching to reach 50% of the prebleaching level within 1 s (Fig. 4, A–C). In comparison, the fluorescence of EGFP-WT actin recovered slowly, reaching 50% of the prebleaching level in ∼5 s and plateauing at ∼88% of the prebleaching level, similar to previous studies (Star et al., 2002; Hotulainen et al., 2009). The EGFP recovery data can be fitted as a single exponential function, resulting in a time constant (τ) of 1.04 s (Fig. 4 D, and Text S1, part 1). However, the EGFP-WT actin data can only be fitted with a double exponential function, resulting in a rapid component (τ_1 = 1.51 s) and a slow component (τ_2 = 44.03 s; Fig. 4 D, and Text S1, part 1), of which the fast component likely represents the diffusible population of WT-actin. As reported previously (Star et al., 2002; Honkura et al., 2008; Hotulainen et al., 2009), the slow component likely represents the dynamic pool of F-actin, whereas the nonrecoverable portion represents the stable F-actin pool. Intriguingly, both EGFP-G13R and EGFP-R62D also exhibited a slow recovery profile, but they were able to completely recover to the prebleaching level (Fig. 4, A–C). Fitted with double exponential functions, both actin mutants exhibited a fast component similar to WT, indicating that the diffusion of these three EGFP-tagged actin proteins is similar (Fig. 4 D, and Text S1, part 1). However, G13R and R62D exhibited a larger time constant (τ_2) for the slow component than WT-actin (69 and

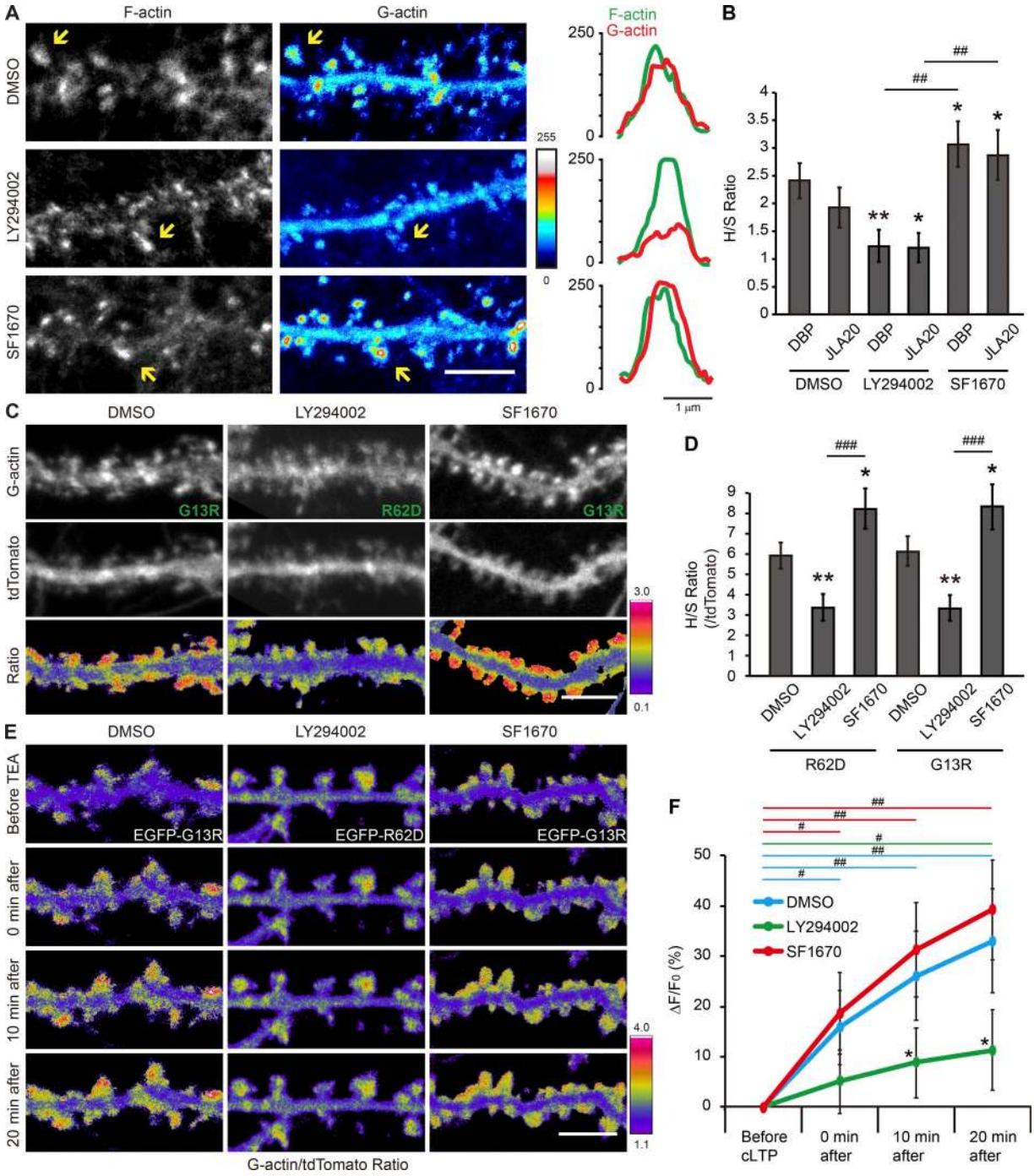

Figure 6. **Inhibition of PI3K and PTEN affects the base-level and activity-dependent G-actin enrichment in dendritic spines differently.** (A) Representative images and fluorescence profiles showing the changes in G-actin levels in spines as revealed by G-actin probes DBP and JLA20 after treatment with PI 3-kinase and PTEN inhibitors. Spines are highlighted by Alexa Fluor 569–phalloidin. The yellow arrows mark some most representative spines of interest. Bar, 5 μm. (B) Quantification of G-actin levels was done in spines by normalizing the spine signals to the adjacent shaft signals. Results were averaged from 25 spines from three batches of culture, and the data distribution was tested for normality with the Shapiro-Wilk test. H/S, spine head to shaft. (C) Representative images of live cells showing the changes in G-actin levels in spines after treatment with PI 3-kinase and PTEN inhibitors. The cells coexpressed either EGFP-R62D or EGFP-G13R with tdTomato as the volume marker, and ratiometric images are shown to highlight the changes in G-actin levels in spines. Bar, 5 μm. (D) Quantification of the G-actin levels in spines from the live-imaging data. Results were averaged from 30 spines from three batches of culture, and the data distribution was tested for normality with the Shapiro-Wilk test. (B and D) $P < 0.001$; two-way ANOVA. Tukey's posthoc test: *, $P < 0.05$; **, $P < 0.01$; DMSO group versus LY294002 or SF1670 treatment group; ##, $P < 0.01$; ###, $P < 0.001$; LY294002 treatment group versus SF1670 treatment group. (E) Representative images showing the changes in G-actin signals in spines after cLTP induction in cells preincubated with PI3-kinase/PTEN inhibitors. Bar, 5 μm. (F) Quantification of the EGFP fluorescence in spines at various times before and after cLTP induction. $P < 0.001$; two-way repeated-measures ANOVA over time. Bonferroni posthoc test: #, $P < 0.05$; ##, $P < 0.01$; DMSO, LY294002, or SF1670 treatment group compared with pre-LTP baseline level; *, $P < 0.05$; LY294002 treatment group versus DMSO group. Results were averaged from 25 spines from three batches of culture, and the data distribution was tested for normality with the Shapiro-Wilk test. Error bars represent the SEM.

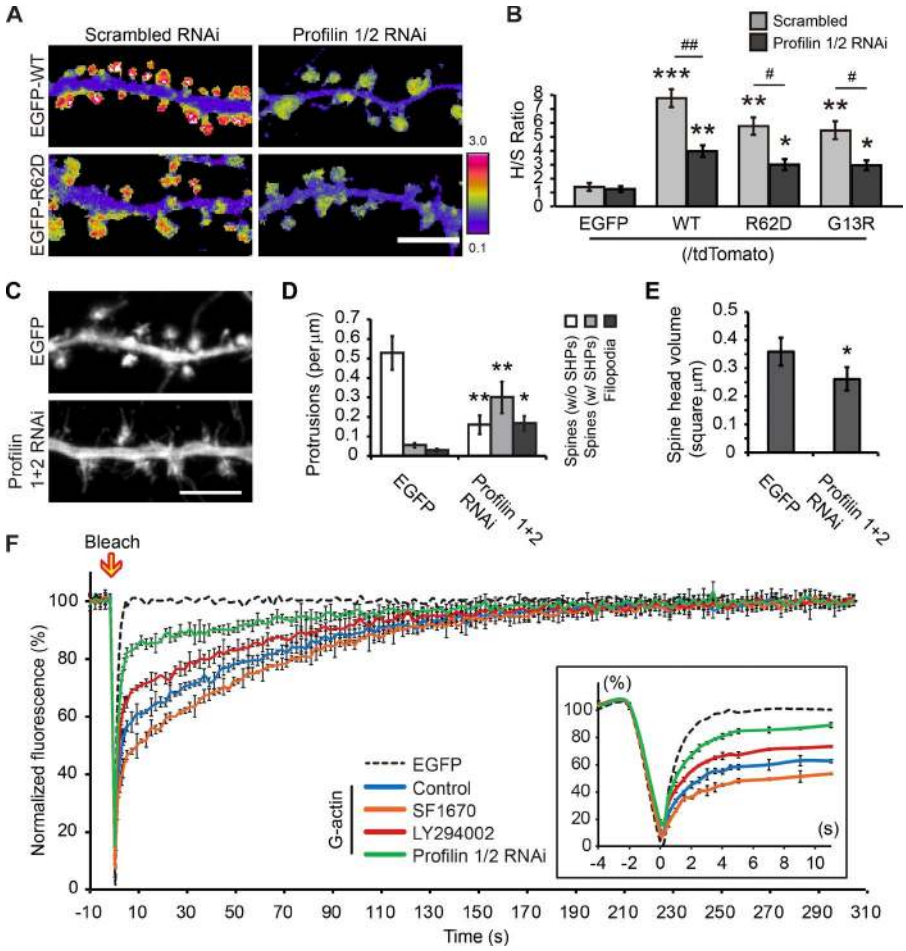

Figure 7. **Knockdown of profilin 1/2 on G-actin enrichment in spines and FRAP analysis of the spine G-actin pool with PI3K/PTEN inhibition or profilin 1/2 knockdown.** (A) Representative ratiometric images of live neurons coexpressing EGFP-WT or EGFP-R62D, tdTomato, and shRNA against either scrambled control or profilin 1/2. The ratios represent EGFP-WT or EGFP-R62D over tdTomato. Bar, 5 µm. (B) Quantification of the difference in G-actin levels in spines from the live-imaging data. The head-to-shaft ratio (H/S ratio) is calculated from normalized EGFP signals (against tdTomato). $P < 0.001$; two-way ANOVA. Tukey's posthoc test: *, $P < 0.05$; **, $P < 0.01$; ***, $P < 0.001$; EGFP group versus WT, R62D, or G13R group; #, $P < 0.05$; ##, $P < 0.01$; WT, R62D, or G13R group expressing scrambled control versus WT, R62D, or G13R group expressing shRNA against profilin 1/2. Results were averaged from 40 spines from three batches of culture, and the data distribution was tested for normality with the Shapiro-Wilk test. (C) Representative images showing the spine morphology in DIV21 hippocampal neurons expressing EGFP + shRNAs. Bar, 5 µm. (D and E) Bar graphs showing the quantification results of spines (with [w/] or without [w/o] SHPs) and filopodia (D) and spine head volume (E) of neurons expressing EGFP + scrambled shRNA or EGFP + shRNA against profilin 1/2. Results were averaged from 45 spines from three batches of culture, and the data distribution was tested for normality with the Shapiro-Wilk test. (D) $P < 0.01$; two-way ANOVA. Tukey's posthoc test: *, $P < 0.05$; **, $P < 0.01$; EGFP group versus profilin 1/2 RNAi group. (E) *, $P < 0.05$; Student's *t* test. (F) FRAP curves for EGFP-R62D of neurons with PI3K/PTEN inhibition by LY294002/SF1670 or profilin 1/2 knockdown. The fluorescent signals in spines are normalized to the prebleaching mean and corrected for the imaging-induced bleaching using the signals from the adjacent shaft regions. The FRAP curve for EGFP is shown as a dashed line for reference. The DMSO treatment group is used as the control. $n = 6$ for each group. Error bars represent the SEM.

70 s vs. 44 s). As both G13R and R62D are nonpolymerizable actin, their slow recovery rates suggest a potential mechanism that might trap and/or immobilize this pool of G-actin in spines.

What potential mechanism could trap/immobilize/enrich G-actin in spines but still allow for removal by mild detergents? One possibility is through interactions with membrane phosphoinositides, especially phosphatidylinositol (4,5)-bisphosphate (PIP_2) and phosphatidylinositol (3,4,5)-triphosphate (PIP_3), which are well known for their roles in synapse development and function (Dotti et al., 2014). PIP_3 in particular has been shown to concentrate in spines where it regulates postsynaptic function and plasticity (Arendt et al., 2010; Ueda and Hayashi, 2013). Therefore, we examined whether the spine enrichment of G-actin is mediated by these two phosphoinositides using EGFP-tagged pleckstrin homology (PH) domains from phospholipase Cδ and AKT kinase to preferentially highlight PIP_2 and PIP_3, respectively. Both EGFP-$PH_{PLC\delta}$δand EGFP-PH_{AKT} highlighted the plasma membrane including dendritic spines, and their signals were diminished after a brief exposure to the detergent saponin (Fig. S5, A–C). This suggests that saponin removes PIP_2 and PIP_3 molecules from neuronal membranes. Furthermore, relatively high expression levels of EGFP-$PH_{PLC\delta}$ or EGFP-PH_{AKT} caused reductions in mushroom-shaped spines (and spine head width) and increases in both filopodia and deformed spines with SHPs (Fig. S5, D–H), similar to the overexpression of nonpolymerizable G-actin mutants. If G-actin enrichment in spines depends on either PIP_2 or PIP_3, we hypothesized that the overexpression of EGFP-tagged PH domains could lead to a reduction in the levels of G-actin in spines by blocking the interaction between G-actin and the phosphoinositides. Indeed, we found that spines expressing EGFP-PH_{AKT} appear to have a reduced level of G-actin, whereas EGFP expression alone has no effect (Fig. 5 A). We further quantitatively examined the correlation between endogenous G-actin levels and the fluorescence of EGFP-$PH_{PLC\delta}$δor EGFP-PH_{AKT} in spines. Whereas expression of EGFP alone had no effect on spine G-actin levels (Fig. 5 B), increasing levels of EGFP-$PH_{PLC\delta}$ and EGFP-PH_{AKT} fluorescence correlated with decreasing levels of endogenous G-actin in spines (Fig. 5, C and D). Neither of these EGFP-PH probes had an effect on ECFP sig-

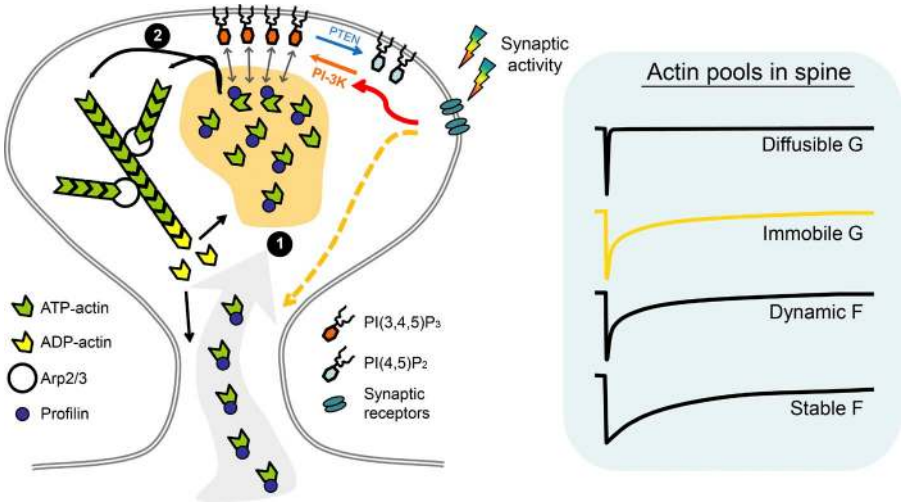

Figure 8. **Schematic model depicting G-actin enrichment in spines.** The local enrichment of G-actin in spines represents an important step that leads to actin polymerization underlying spine enlargement during synapse development and plasticity. The enrichment of G-actin is mediated, in part, by the actin monomer–binding protein profilin. The G-actin pool in spines is relatively immobile because of its association with PIP_3, although the exact molecular details remain to be determined. Synaptic activities regulate G-actin enrichment in spines by affecting the PIP_3 level through PI-3 kinase. The boxed panel summarizes the different pools of actin proteins in spines represented by the recovery curves after photobleaching. The diffusible G-actin, dynamic F-actin, and stable F-actin pools have been established previously. Our data indicate the existence of a relatively immobile pool of G-actin in spines.

nals in spines (Fig. 5, E and F). However, the effect of EGFP-PH_{AKT} on spine G-actin signals is approximately three times that of EGFP-$PH_{PLC\delta}$ (based on the slopes of the regression lines of the correlation plots; Fig. 5, C and D), suggesting that PIP_3 is the primary phosphoinositide involved in mediating G-actin enrichment in spines. We further confirmed these findings using live imaging of mCherry-G13R or mCherry-R62D coexpressed with EGFP-$PH_{PLC\delta}$ or EGFP-$PH_{AKT.}$ Consistently, EGFP-PH_{AKT} exerted a much stronger inhibition on the spine enrichment of these actin mutants than EGFP-$PH_{PLC\delta}$ (Fig. 5, G and H).

To better interpret our experimental findings concerning $PH_{PLC\delta}$ and PH_{AKT} expression on G-actin in spines, we considered alternative computational models that relate $PH_{PLC\delta}$, PH_{AKT}, and G-actin through competition for availability of PIP_2 and PIP_3 (Fig. S6, and Text S1, part 2). We tested four different competition models, in which either G-actin or a PH domain can form a scaffold with PIP_2 or PIP_3 but not both (Fig. S6, A–C). We found that only the models including the formation of a ternary scaffold with PIP_3, PH_{AKT}, and G-actin (Fig. S6 C) fit both weak and strong correlation curves from Fig. 5 (C and D), as shown by the least square optimization fitting with MATLAB (Fig. S6 D). This result explains the high sensitivity of G-actin accumulation in spines to the presence of the PH_{AKT} domain and supports the competition mechanism where there is a much stronger interaction between G-actin and PIP_3 than with PIP_2. Together, these results support the notion that PIP_3 mediates G-actin enrichment in spines, and it represents an important mechanism underlying dynamic F-actin assembly during spine development and plasticity.

The cellular levels of PIP_3 and PIP_2 are regulated by PI-3 kinase (PI3K; phosphatidylinositide 3-kinase) and PTEN (phosphatase and tensin homologue). Therefore, we examined whether pharmacological manipulation of PI3K and PTEN can alter G-actin enrichment in dendritic spines. We found that inhibition of PI3K using LY294002 (Vlahos et al., 1994) resulted in a marked reduction in the spine enriched pool of endogenous G-actin, whereas PTEN inhibition by SF1670 (Rosivatz et al., 2006) led to an increase in spine G-actin (Fig. 6, A and B). Similar results were obtained from live-cell imaging of EGFP-G13R and EGFP-R62D (Fig. 6, C and D). Furthermore, inhibition of PI3K but not PTEN suppressed the TEA-cLTP–induced increase of G-actin in spines (Fig. 6, E and F). Given that PI3K is known to be activated by synaptic signaling (Man et al., 2003; Sui et al., 2008), these results link synaptic signaling to the PIP_3-mediated enrichment of G-actin in spines for activity-dependent changes in spine size.

Phosphoinositides play an important role in the spatiotemporal regulation of the actin cytoskeleton and its dynamics (Saarikangas et al., 2010), in part through interactions with actin monomer–binding proteins such as profilin (Paavilainen et al., 2004). Interestingly, the actin monomer–binding protein profilin has been shown to undergo activity-dependent trafficking into spines (Ackermann and Matus, 2003; Neuhoff et al., 2005). To explore the possible involvement of actin monomer–binding

Table 1. **FRAP of EGFP-R62D/G13R in dendritic spines under different conditions**

	GFP-actin	50% Prebleaching	50% plateau	90% plateau	99% plateau	Plateau at 300 s (%)
DMSO	G13R	3.1 ± 0.3	3.0 ± 0.3	100 ± 5.5	249 ± 16	99 ± 0.62
	R62D	3.0 ± 0.4	3.0 ± 0.3	101 ± 5.8	248 ± 15	99 ± 0.84
LY294002	G13R	1.7 ± 0.3	1.7 ± 0.2	85 ± 4.3	221 ± 13	99 ± 0.82
	R62D	1.8 ± 0.2	1.8 ± 0.2	84 ± 4.7	223 ± 14	99 ± 0.99
SF1670	G13R	10.0 ± 0.3	9.4 ± 0.3	116 ± 6.9	274 ± 16	99 ± 0.51
	R62D	9.4 ± 0.4	9.2 ± 0.3	115 ± 7.2	272 ± 17	99 ± 0.56
Scramble RNAi	G13R	3.1 ± 0.3	3.1 ± 0.2	99 ± 6.0	253 ± 16	99 ± 0.53
	R62D	3.1 ± 0.2	3.1 ± 0.2	100 ± 5.7	260 ± 15	99 ± 0.56
Profilin 1/2 RNAi	G13R	1.2 ± 0.3	1.1 ± 0.3	40 ± 4.2	173 ± 14	99 ± 0.95
	R62D	1.2 ± 0.3	1.2 ± 0.2	38 ± 4.5	169 ± 13	99 ± 1.00

Quantification table showing recovery time for 50% prebleaching levels, 50% plateau levels, 90% and 99% plateau levels, and the final recovery percentages of EGFP-R62D/G13R in dendritic spines under different conditions. All numbers are presented in seconds as mean ± SEM.

Table 2. **Curve fitting of FRAP data**

	GFP-actin	F(0)	F(e)	c	τ1 (sec)	τ2 (sec)
Control	WT	0.0960	0.8797	0.4161	1.5112	44.0287
	G13R	0.1041	1.0019	0.4637	1.4744	69.3191
	R62D	0.1021	1.0002	0.4506	1.5724	70.2468
DMSO	G13R	0.10126	1.0006	0.45883	1.5190	69.4147
	R62D	0.098472	1.0035	0.45535	1.5174	72.7302
LY294002	G13R	0.1274	1.0004	**0.34306↓**	1.3793	69.8583
	R62D	0.16293	0.99987	**0.3464↓**	1.4974	68.949
SF1670	G13R	0.087312	0.9997	0.57153↑	1.6203	70.3258
	R62D	0.081741	1.0016	0.57138↑	1.5003	70.0223
Scramble RNAi	G13R	0.099384	0.99966	0.45277	1.5389	70.3558
	R62D	0.098478	1.0030	0.45301	1.5687	72.6469
Profilin 1/2 RNAi	G13R	0.16664	0.9999	**0.17228↓**	1.5483	72.8719
	R62D	0.16208	1.0016	**0.17482↓**	1.5657	74.7082

The comprehensive table summarizes all five parameters (F[0], F[e], c, τ1, and τ2) of the double exponential function used to fit the FRAP curves of WT actin or actin mutants. Note that τ1 and τ2 are similar among actin mutants under different conditions. Arrows indicate the changes with bold numbers depicting an increase over the control.

proteins in G-actin enrichment in dendritic spines, we knocked down both profilin 1 and 2 (hereafter referred to as profilin 1/2) using shRNA. We observed a large reduction in G-actin levels in dendritic spines (Fig. 7, A and B). Importantly, knockdown of profilin 1/2 reduced the number of mushroom-shaped spines and spine head volume and increased the number of both deformed spines with SHPs and filopodia, without affecting the total number of dendritic protrusions (Fig. 7, C–E).

Finally, we performed FRAP to examine the recovery kinetics of actin mutants when the PIP_3 level was altered or profilin 1/2 was knocked down (Fig. 7 F and Table 1). Consistently, 30-min inhibition of PI-3K resulted in a faster recovery of both actin mutants, whereas PTEN inhibition slowed the recovery. Remarkably, knockdown of profilin 1/2 had the most profound effect, resulting in a much faster recovery of both actin mutants. To gain further insights into the underlying mechanism, we again performed the curve fitting and found that all these recovery data can only be adequately fitted with a double exponential function (Table 2). Despite the different manipulations, all FRAP data contain a rapid component and a slow component with their time constants ($\tau_1 \approx 1.5$ s and $\tau_2 \approx 70$ s) consistent across the data (Table 2), indicating that the recovery kinetics of these two G-actin pools was not altered. However, PI-3K inhibition appears to have reduced the size of the slow component pool. This is indicated by the reduced contribution of this component to the fit, which is reflected by the smaller value of the corresponding preexponential constant c (Text S1, part 1). However, PTEN inhibition resulted in an increased c, suggesting that the size of the slow component pool was increased. Knockdown of profilin 1/2 had the most profound reduction in the pool of the slow component, as the constant c is about three times smaller than that of the scramble control (Table 2). Together with the reduction in the amount of G-actin in spines after profilin knockdown or PI-3K inhibition, these results provide strong support to our model in which profilin molecules are involved in the PIP3-mediated spine enrichment of G-actin in dendritic spines (Fig. 8). Given that several actin regulatory proteins have been shown to undergo activity-dependent translocation into spines (Bosch et al., 2014), it is likely that the local concentration of G-actin and its assembly into distinct F-actin structures in spines involve the concerted actions of many actin regulatory proteins. Nonetheless, our findings show a novel actin mechanism by which spatiotemporal regulation of G-actin in spines regulates F-actin assembly and dynamic remodeling during synapse formation and plasticity.

Discussion

The unique morphology of dendritic spines enables them to function as isolated electrical and biochemical compartments, thereby permitting individual synapses to function independently during information storage and processing. The separation of the spine head from the dendritic shaft by the narrow spine neck has been shown to limit the diffusion of some molecules and allow for the compartmentalization of calcium and neurotransmitter receptor signaling (Majewska et al., 2000; Sabatini et al., 2002; Noguchi et al., 2005; Tønnesen et al., 2014). However, this means that, for certain molecules, particularly those required for rapid activity-dependent modifications, it may be advantageous to be locally available rather than recruited on demand from the dendritic shaft. In this study, we present evidence for a novel actin mechanism in which spatiotemporal enrichment of G-actin in spines regulates normal spine development and plasticity-induced changes in spine morphology. Our data further reveal that the local enrichment of G-actin in spines depends on the phosphoinositide PIP_3 and is regulated by PI3K and PTEN, which are known to play a crucial role in mediating synaptic signaling and plasticity (Dotti et al., 2014). Importantly, our results suggest that actin assembly during spine enlargement occurs in two distinct steps: (1) the local enrichment of G-actin and (2) its subsequent polymerization into F-actin (see Fig. 8). Finally, our data suggest that the spine enrichment of G-actin involves actin monomer–binding proteins such as profilin. Considering that mutations and altered expression of profilin are associated with several neurological disorders (Wu et al., 2012; Michaelsen-Preusse et al., 2016), our findings support an important role of the spatiotemporal regulation of actin monomers in synapse development and may potentially provide the insights into the cellular mechanisms underlying these neurological disorders.

Previous studies examining the dynamics of actin in spines have largely focused on F-actin, while making the assumption that G-actin is readily diffusible (Star et al., 2002; Honkura et al., 2008; Frost et al., 2010). At least two

pools of F-actin have been identified: a dynamic pool that represents the dynamic turnover of F-actin through treadmilling and a relatively stable pool at the base of spine heads that likely plays a role in stabilizing spines (Star et al., 2002; Honkura et al., 2008; Frost et al., 2010). Honkura et al. also identified an enlargement pool with an intermediate time constant that is confined to the spine head by the spine neck and is responsible for spine enlargement. Considering the ∼10:1 ratio of F- to G-actin in the spine and the longer time constant of this pool (Honkura et al., 2008), it is possible that some fraction of the enlargement pool of F-actin may include the enriched G-actin described here. We propose refining this model to include the relatively immobile pool of G-actin that is confined to the spine head by PIP_3. The time constant of this pool of G-actin is longer than the dynamic pool of F-actin, which suggests that it may function in activity-dependent rapid spine expansion or provide a reservoir to capture G-actin from rapidly depolymerizing filaments (see Fig. 8). Superresolution microscopy has recently been used to identify independently regulated distinct F-actin networks within spine subdomains, and future studies using this method using G-actin mutants could shed light on where monomers are incorporated and reveal whether G-actin is confined by the spine neck.

In cells, G-actin is bound by families of actin monomer–binding proteins that regulate its nucleotide state, availability for polymerization, and interactions with other actin regulatory proteins (Paavilainen et al., 2004). Here, we show that profilin is required for the enrichment of G-actin in spines and that its knockdown results in the loss of mushroom-shaped spines. This suggests a role for profilin in G-actin enrichment in the spine head and possibly in mediating an interaction with phosphoinositides. Profilin is able to directly bind both PIP_2 and PIP_3, but this interaction could result in the loss of its ability to bind actin monomers (Saarikangas et al., 2010). Therefore, the spine enrichment of G-actin may not be a result of direct PIP_3 association of the profilin–actin complex. Instead, it is possible that profilin–actin complexes may interact with PIP_3 through another protein, like a member of the Wiskott–Aldrich syndrome protein family (Takenawa and Suetsugu, 2007). Future studies are needed to fully elucidate the molecular details that enable PIP_3-mediated local enrichment of G-actin in dendritic spines.

It should be noted that of the six mammalian actins, β and γ cytoplasmic actin are the isoforms found in neurons and only differ by four biochemically similar amino acids at the amino-terminal region. Previous studies suggest that both γ-actin and β-actin are found in spines, although there appears to be some age- and brain region–specific differences in their localization patterns (Kaech et al., 1997; Cheever and Ervasti, 2013). Although our live imaging used GFP-tagged γ-actin to show the activity-dependent spine enrichment of G-actin, β-actin likely exhibits a similar spine enrichment pattern as we have shown a similar localization of both γ– and β–G-actin in the leading edge of motile growth cones (Lee et al., 2013). However, given that β-actin is often found in dynamic structures, the ratio of γ-actin and β-actin in spines may vary depending on the developmental stages of the spines. Nonetheless, our findings have uncovered a new mechanism by which dynamic enrichment of G-actin in spines regulates actin assembly and spine remodeling during development and plasticity.

Materials and methods

DNA constructs, antibodies, and reagents

The following DNA constructs were used in this study: pcDNA3-EGFP, pcDNA3-ECFP, EGFP-actin (pCS2+ EGFP–γ-actin), EGFP-actin$_{R62D}$ (pCS2+ EGFP–γ-actin$_{R62D}$), EGFP-actin$_{G13R}$ (pCS2+ EGFP–γ-actin$_{G13R}$), mCherry-actin$_{R62D}$ (pCS2+ mCherry–γ-actin$_{R62D}$), mCherry-actin$_{G13R}$ (pCS2+ mCherry–γ-actin$_{G13R}$), pLVX-IRES-tdTomato, EGFP-C1-PH$_{PLCδ}$, EGFP-C1-PH$_{AKT}$, pCAG–PSD-95–tdTomato, and pSUPER for shRNA expression. The shRNA sequences used in this study are (all in the 5′-3′ direction): profilin 1, GCAAAGACCGGTCAAGTTT; and profilin 2, GTAGAGCATTGGTTATAGT. DNA constructs were prepared using the PureLink HiPure Plasmid Maxiprep kit (K2100) from Invitrogen (Thermo Fisher Scientific).

Gc-globulin from human plasma (DBP) was from Sigma-Aldrich (G8764). Rabbit polyclonal anti–human Gc-globulin antibody (A0021) was from Dako (Agilent Technologies). Mouse monoclonal anti-actin antibody (Ab-1; JLA20) was from Calbiochem (EMD Millipore). Mouse monoclonal anti-PSD95 antibody (MA1-045) and Alexa Fluor secondary antibodies were from Thermo Fisher Scientific.

All restriction enzymes were from New England BioLabs or Fermentas (Thermo Fisher Scientific). Alexa Fluor 546 phalloidin (A22283) was from Invitrogen (Thermo Fisher Scientific). DAPI (10236276001) was from Roche Life Science. DMSO (D8418), saponin (47036), TEA chloride (T2265), and L-glutamic acid (G1251) were from Sigma-Aldrich. PFA (18814) was from Polysciences, Inc. Prototypical PI 3-kinase inhibitor LY294002 (1130) and PTEN inhibitor SF1670 (5020) were from Tocris Bioscience.

Animal care

All animals were treated in accordance with the Emory University Institutional Animal Care and Use Committee guidelines.

Dissociated hippocampal neuron culture

All coverslips for hippocampal neuron cultures were coated with 0.1 mg/ml poly-D-lysine 24 h before dissection. Hippocampi from E18 rat embryos were digested with 0.125% trypsin-EDTA for 25 min at 37°C, followed by trituration with pipettes in the neuronal culture media (neurobasal medium containing 1% glutamate and 2% B27 supplement). The neuronal culture was kept at 37°C and 5% CO_2 in an incubator thereafter. Then, one third of the neuronal culture media was changed every 72 h.

Rodent hippocampal slice culture

Brain slice culture was performed by following the method described previously (Fuller and Dailey, 2007). In brief, P5 rat hippocampi were cut into 300-µm coronal sections by a tissue chopper after being cut free from the cerebral hemispheres. Then, the slices were separated and cultured on culture plate inserts (Millipore) in MEM containing 25% HBSS, 6.5 mg/ml D-glucose, 25% horse serum, and 1% penicillin-streptomycin in a humidified CO_2 incubator.

Immunocytochemistry

Neurons were first washed with PBS (5% glucose) and then fixed in 4% paraformaldehyde at RT for 30 min and incubated with 0.1% Triton X-100 in PBS (5% glucose) for 10 min. After blocking with 8% goat serum and 1% BSA in PBS (5% glucose) at RT for 1 h, neurons were incubated in primary antibodies at 4°C for >12 h and subsequently with Alexa Fluor secondary antibodies at RT for 2 h. Coverslips were mounted with Fluoromount-G mounting medium from SouthernBiotech before observation.

Calcium phosphate transfection

A CalPhos transfection kit (Clontech-Takara) was used. For each 35-mm culture dish, 2–4 µg DNA, water, and 5 µl of 2 M $CaCl_2$ were mixed into a 40-µl total volume. This solution was added into 40 µl of 2× Hepes-buffered saline dropwise while continuously vortexing. The mixed solution was added to neurons after 20-min RT incubation. After that, the neurons were incubated at 37°C and 5% CO_2 for 30–40 min and washed with plain neurobasal medium before being put back into the incubator for another 45–60 min. Finally, the neurobasal medium was removed, and the normal culture medium was added back. Dissociated hippocampal neurons were transfected at DIV13 and then imaged and analyzed at DIV21, unless stated otherwise.

Live-cell imaging

Neurons were changed from culture medium to a Hepes-buffered recording solution (140 mM NaCl, 5 mM KCl, 2 mM $CaCl_2$, 1.5 mM $MgCl_2$, 10 mM glucose, and 25 mM Hepes, pH 7.4). Coverslips with neurons were mounted onto a heating chamber and maintained at 37°C during imaging. Most of the imaging experiments were performed on a confocal system (C1; Nikon) using an oil objective (NA = 1.4; 60×; Plan Apo). For all the cells, we use the same optical settings (laser power, pinhole size, gain, etc.) for image acquisition, so their fluorescence can be compared. FRAP experiments were done on an A1R confocal system (Nikon) using an oil objective (NA = 1.49; CFI Apo TIRF 60×) with a stage incubator (37°C and 5% CO_2).

Biolistic transfection of neurons in slice culture

Biolistic transfection was performed as previously defined (McAllister, 2000; Woods and Zito, 2008). In short, up to 50 µg of DNA was precipitated on 6–8 mg of gold powders (0.3–3 µm; Crescent Chemical Co., Inc.) by adding 100 µl of 1 M $CaCl_2$. Then, the gold/DNA pellet was resuspended in 3.5 ml polyvinylpyrrolidone (Sigma-Aldrich) solution. After that, Tefzel tubing was coated with the gold/polyvinylpyrrolidone solution, dried in the tubing station (Bio-Rad), and cut into bullets. Finally, brain slices were shot from 0.5–1 inches away using a Helios gene gun (Bio-Rad) connected to a helium gas tank (180 PSI). Rat hippocampal slices were transfected at DIV3 and then imaged and analyzed at DIV6.

Saponin extraction, LTP induction, and enzyme inhibitors application

Live-cell extraction was conducted by treating cells with a permeabilization buffer (20 mM Hepes, 138 mM KCl, 4 mM $MgCl_2$, 3 mM EGTA, 1% BSA, 1 mM ATP, 3 µM phalloidin, and 0.2 mg/ml saponin) for 60 s, followed by immediate fixation or imaging.

For TEA-cLTP, we briefly exposed the neurons to the TEA solution for 10 min, as described previously (Gu et al., 2010). The TEA solution is based on the recording solution but contains 5 mM $CaCl_2$, 0.1 mM $MgCl_2$, and 25 mM TEA (Sigma-Aldrich). For glutamate-induced cLTP, we followed the previously described protocol (Ackermann and Matus, 2003) and treated the neurons with 10 µM L-glutamate in Mg^{2+}-free Hepes-buffered solution (142 mM NaCl, 5 mM KCl, 2 mM $CaCl_2$, 10 mM glucose, and 25 mM Hepes, pH 7.4) for 30 min.

Inhibition of PI 3-kinase and PTEN were performed by adding 40 µM LY294002 and 60 µM SF1670 2 h or 30 min before proceeding with studies of baseline distribution or synaptic activity-dependent localization of G-actin in dendritic spines, respectively.

FRAP

The FRAP assay was conducted on an A1R laser-scanning confocal microscope equipped with an automated z drive with Perfect Focus, multiple laser lines with acousto-optic tunable filter control, a motorized x-y stage, an attached cage incubator with CO_2 and temperature control, and multiple photomultiplier tube detectors. Cells were mounted in a custom live-cell chamber. All experiments were performed using an oil immersion objective (60× 1.49NA PlanApoN TIRF). First, six control images at one frame per second were acquired. Photobleaching was done by using a region of interest that enclosed a single spine head with the maximal power of the 488-nm laser line from a 40-mW argon laser. The bleaching duration was 500 ms, and pixel dwell was set at 3.9 µs. Immediately after photobleaching, a 5-s imaging sequence was acquired with no delay between frames, yielding nine frames. A second sequence of 150 images was followed with a 2-s interval between frames. Imaging was done using the following settings: 488-nm laser power = 2%, pixel dwell = 1.2 µs, and resolution = 0.07 µm/pixel.

Image processing and statistical analysis

Data analyses were performed using ImageJ (National Institutes of Health) and NIS-Elements software. Dendritic regions of interest in hippocampal neurons were first taken as three-dimensional image stacks and then projected to two-dimensional images using the maximal intensity z-projection function from ImageJ. To analyze spine volume, we measured the integrated intensity of tdTomato or EGFP signals in all the spines selected by the Auto Thresholding function from ImageJ. Ratio images were made with a custom Ratio ImageJ Plugin after background subtraction, registration, and photobleaching correction. For FRAP assay data analysis, images were background subtracted and corrected for photobleaching. Fluorescence intensity profiles of dendritic spines were generated along 5 pixel–wide lines through the centers of dendritic spine heads of interest with the plot profile tool of ImageJ. Sholl analysis was performed by using the Anirvan Ghosh laboratory ImageJ Sholl Analysis Plugin (v1.0). Most statistical analysis was performed using SPSS Statistics (v.24; IBM Corp.).

To determine the effects of exogenously expressed EGFP-actin or EGFP-actin mutants on cells, we grouped them into two groups according to the mean EGFP fluorescence intensity of their cell bodies: low-expression group < 1,500 and high-expression group > 2,500. Immunostaining of the total actin proteins using a pan-actin antibody (Ab14128; Abcam) was used to estimate the amount of overexpression of these EGFP-tagged actin proteins relative to the endogenous level.

Online supplemental material

Fig. S1 shows live-cell extraction of G-actin in spines by saponin and correlation between G-actin and PSD95 in spines. Fig. S2 shows enrichment of G-actin in dendritic spines of hippocampal neurons in organotypic brain slices. Fig. S3 shows actin expression level, total protrusion number, spine neck length, PSD95 signals, and dendritic arborization of neurons expressing different levels of EGFP, EGFP-WT, EGFP-G13R, and EGFP-R62D. Fig. S4 shows activity-dependent G-actin enrichment in dendritic spines during glutamate-induced synaptic potentiation. Fig. S5 shows live-cell extraction of PIP_2 and PIP_3 by saponin and expression of EGFP-$PH_{PLC\delta}$ or EGFP-PH_{AKT} on spine development and synapse formation. Fig. S6 shows alternative models of G-actin interaction with phosphoinositides and the resulting fit to experimental data. Text S1 is available as a PDF and shows details of curve fitting of FRAP data and models for binding competition between G-actin and PH domains for association with the inositol lipids PI(*4,5*)P_2 and PI(*3,4,5*)P_3.

Acknowledgments

This project is supported in part by research grants from the National Institutes of Health to J.Q. Zheng (MH104632 and GM083889), a Ruth L. Kirschstein National Research Service Award Postdoctoral Fellowship to K.R. Myers (NS092342), and a National Institute of Neu-

rological Disorders and Stroke core facilities grant (P30NS055077) to the Integrated Cellular Imaging Microscopy Core of Emory University.

The authors declare no competing financial interests.

Author contributions: W. Lei performed most of the experiments and data analyses. K.R. Myers helped with the brain slice work, and Y. Rui performed some of the imaging experiments. S. Hladyshau and D. Tsygankov performed the curve fitting and computational modeling of the data. J.Q. Zheng planned and oversaw the project. W. Lei, K.R. Myers, and J.Q. Zheng wrote the manuscript.

Submitted: 7 December 2016
Revised: 3 April 2017
Accepted: 18 May 2017

References

Ackermann, M., and A. Matus. 2003. Activity-induced targeting of profilin and stabilization of dendritic spine morphology. *Nat. Neurosci.* 6:1194–1200. http://dx.doi.org/10.1038/nn1135

Arendt, K.L., M. Royo, M. Fernández-Monreal, S. Knafo, C.N. Petrok, J.R. Martens, and J.A. Esteban. 2010. PIP_3 controls synaptic function by maintaining AMPA receptor clustering at the postsynaptic membrane. *Nat. Neurosci.* 13:36–44. http://dx.doi.org/10.1038/nn.2462

Bloodgood, B.L., and B.L. Sabatini. 2005. Neuronal activity regulates diffusion across the neck of dendritic spines. *Science.* 310:866–869. http://dx.doi.org/10.1126/science.1114816

Bosch, M., J. Castro, T. Saneyoshi, H. Matsuno, M. Sur, and Y. Hayashi. 2014. Structural and molecular remodeling of dendritic spine substructures during long-term potentiation. *Neuron.* 82:444–459. http://dx.doi.org/10.1016/j.neuron.2014.03.021

Cheever, T.R., and J.M. Ervasti. 2013. Actin isoforms in neuronal development and function. *Int. Rev. Cell Mol. Biol.* 301:157–213. http://dx.doi.org/10.1016/B978-0-12-407704-1.00004-X

Chhabra, E.S., and H.N. Higgs. 2007. The many faces of actin: matching assembly factors with cellular structures. *Nat. Cell Biol.* 9:1110–1121. http://dx.doi.org/10.1038/ncb1007-1110

Dotti, C.G., J.A. Esteban, and M.D. Ledesma. 2014. Lipid dynamics at dendritic spines. *Front. Neuroanat.* 8:76. http://dx.doi.org/10.3389/fnana.2014.00076

Frost, N.A., H. Shroff, H. Kong, E. Betzig, and T.A. Blanpied. 2010. Single-molecule discrimination of discrete perisynaptic and distributed sites of actin filament assembly within dendritic spines. *Neuron.* 67:86–99. http://dx.doi.org/10.1016/j.neuron.2010.05.026

Fuller, L., and M.E. Dailey. 2007. Preparation of rodent hippocampal slice cultures. *CSH Protoc.* 2007:t4848.

Geinisman, Y. 2000. Structural synaptic modifications associated with hippocampal LTP and behavioral learning. *Cereb. Cortex.* 10:952–962. http://dx.doi.org/10.1093/cercor/10.10.952

Gu, J., B.L. Firestein, and J.Q. Zheng. 2008. Microtubules in dendritic spine development. *J. Neurosci.* 28:12120–12124. http://dx.doi.org/10.1523/JNEUROSCI.2509-08.2008

Gu, J., C.W. Lee, Y. Fan, D. Komlos, X. Tang, C. Sun, K. Yu, H.C. Hartzell, G. Chen, J.R. Bamburg, and J.Q. Zheng. 2010. ADF/cofilin-mediated actin dynamics regulate AMPA receptor trafficking during synaptic plasticity. *Nat. Neurosci.* 13:1208–1215. http://dx.doi.org/10.1038/nn.2634

Halpain, S., K. Spencer, and S. Graber. 2005. Dynamics and pathology of dendritic spines. *Prog. Brain Res.* 147:29–37. http://dx.doi.org/10.1016/S0079-6123(04)47003-4

Honkura, N., M. Matsuzaki, J. Noguchi, G.C. Ellis-Davies, and H. Kasai. 2008. The subspine organization of actin fibers regulates the structure and plasticity of dendritic spines. *Neuron.* 57:719–729. http://dx.doi.org/10.1016/j.neuron.2008.01.013

Hotulainen, P., and C.C. Hoogenraad. 2010. Actin in dendritic spines: connecting dynamics to function. *J. Cell Biol.* 189:619–629. http://dx.doi.org/10.1083/jcb.201003008

Hotulainen, P., O. Llano, S. Smirnov, K. Tanhuanpää, J. Faix, C. Rivera, and P. Lappalainen. 2009. Defining mechanisms of actin polymerization and depolymerization during dendritic spine morphogenesis. *J. Cell Biol.* 185:323–339. http://dx.doi.org/10.1083/jcb.200809046

Johnson, O.L., and C.C. Ouimet. 2006. A regulatory role for actin in dendritic spine proliferation. *Brain Res.* 1113:1–9. http://dx.doi.org/10.1016/j.brainres.2006.06.116

Kaech, S., M. Fischer, T. Doll, and A. Matus. 1997. Isoform specificity in the relationship of actin to dendritic spines. *J. Neurosci.* 17:9565–9572.

Korobova, F., and T. Svitkina. 2010. Molecular architecture of synaptic actin cytoskeleton in hippocampal neurons reveals a mechanism of dendritic spine morphogenesis. *Mol. Biol. Cell.* 21:165–176. http://dx.doi.org/10.1091/mbc.E09-07-0596

Lee, C.W., E.A. Vitriol, S. Shim, A.L. Wise, R.P. Velayutham, and J.Q. Zheng. 2013. Dynamic localization of G-actin during membrane protrusion in neuronal motility. *Curr. Biol.* 23:1046–1056. http://dx.doi.org/10.1016/j.cub.2013.04.057

Majewska, A., A. Tashiro, and R. Yuste. 2000. Regulation of spine calcium dynamics by rapid spine motility. *J. Neurosci.* 20:8262–8268.

Man, H.Y., Q. Wang, W.Y. Lu, W. Ju, G. Ahmadian, L. Liu, S. D'Souza, T.P. Wong, C. Taghibiglou, J. Lu, et al. 2003. Activation of PI3-kinase is required for AMPA receptor insertion during LTP of mEPSCs in cultured hippocampal neurons. *Neuron.* 38:611–624. http://dx.doi.org/10.1016/S0896-6273(03)00228-9

McAllister, A.K. 2000. Biolistic transfection of neurons. *Sci. STKE.* 2000:pl1.

Michaelsen-Preusse, K., S. Zessin, G. Grigoryan, F. Scharkowski, J. Feuge, A. Remus, and M. Korte. 2016. Neuronal profilins in health and disease: Relevance for spine plasticity and Fragile X syndrome. *Proc. Natl. Acad. Sci. USA.* 113:3365–3370. http://dx.doi.org/10.1073/pnas.1516697113

Neuhoff, H., M. Sassoè-Pognetto, P. Panzanelli, C. Maas, W. Witke, and M. Kneussel. 2005. The actin-binding protein profilin I is localized at synaptic sites in an activity-regulated manner. *Eur. J. Neurosci.* 21:15–25. http://dx.doi.org/10.1111/j.1460-9568.2004.03814.x

Nimchinsky, E.A., B.L. Sabatini, and K. Svoboda. 2002. Structure and function of dendritic spines. *Annu. Rev. Physiol.* 64:313–353. http://dx.doi.org/10.1146/annurev.physiol.64.081501.160008

Noguchi, J., M. Matsuzaki, G.C. Ellis-Davies, and H. Kasai. 2005. Spine-neck geometry determines NMDA receptor-dependent Ca^{2+} signaling in dendrites. *Neuron.* 46:609–622. http://dx.doi.org/10.1016/j.neuron.2005.03.015

Paavilainen, V.O., E. Bertling, S. Falck, and P. Lappalainen. 2004. Regulation of cytoskeletal dynamics by actin-monomer-binding proteins. *Trends Cell Biol.* 14:386–394. http://dx.doi.org/10.1016/j.tcb.2004.05.002

Penzes, P., M.E. Cahill, K.A. Jones, J.E. VanLeeuwen, and K.M. Woolfrey. 2011. Dendritic spine pathology in neuropsychiatric disorders. *Nat. Neurosci.* 14:285–293. http://dx.doi.org/10.1038/nn.2741

Pollard, T.D., and G.G. Borisy. 2003. Cellular motility driven by assembly and disassembly of actin filaments. *Cell.* 112:453–465. http://dx.doi.org/10.1016/S0092-8674(03)00120-X

Pollard, T.D., L. Blanchoin, and R.D. Mullins. 2000. Molecular mechanisms controlling actin filament dynamics in nonmuscle cells. *Annu. Rev. Biophys. Biomol. Struct.* 29:545–576. http://dx.doi.org/10.1146/annurev.biophys.29.1.545

Posern, G., A. Sotiropoulos, and R. Treisman. 2002. Mutant actins demonstrate a role for unpolymerized actin in control of transcription by serum response factor. *Mol. Biol. Cell.* 13:4167–4178. http://dx.doi.org/10.1091/mbc.02-05-0068

Rosivatz, E., J.G. Matthews, N.Q. McDonald, X. Mulet, K.K. Ho, N. Lossi, A.C. Schmid, M. Mirabelli, K.M. Pomeranz, C. Erneux, et al. 2006. A small molecule inhibitor for phosphatase and tensin homologue deleted on chromosome 10 (PTEN). *ACS Chem. Biol.* 1:780–790. http://dx.doi.org/10.1021/cb600352f

Saarikangas, J., H. Zhao, and P. Lappalainen. 2010. Regulation of the actin cytoskeleton-plasma membrane interplay by phosphoinositides. *Physiol. Rev.* 90:259–289. http://dx.doi.org/10.1152/physrev.00036.2009

Sabatini, B.L., T.G. Oertner, and K. Svoboda. 2002. The life cycle of Ca^{2+} ions in dendritic spines. *Neuron.* 33:439–452. http://dx.doi.org/10.1016/S0896-6273(02)00573-1

Segal, M. 2005. Dendritic spines and long-term plasticity. *Nat. Rev. Neurosci.* 6:277–284. http://dx.doi.org/10.1038/nrn1649

Star, E.N., D.J. Kwiatkowski, and V.N. Murthy. 2002. Rapid turnover of actin in dendritic spines and its regulation by activity. *Nat. Neurosci.* 5:239–246. http://dx.doi.org/10.1038/nn811

Sui, L., J. Wang, and B.M. Li. 2008. Role of the phosphoinositide 3-kinase-Akt-mammalian target of the rapamycin signaling pathway in long-term potentiation and trace fear conditioning memory in rat medial prefrontal cortex. *Learn. Mem.* 15:762–776. http://dx.doi.org/10.1101/lm.1067808

Takenawa, T., and S. Suetsugu. 2007. The WASP-WAVE protein network: connecting the membrane to the cytoskeleton. *Nat. Rev. Mol. Cell Biol.* 8:37–48. http://dx.doi.org/10.1038/nrm2069

Tønnesen, J., G. Katona, B. Rózsa, and U.V. Nägerl. 2014. Spine neck plasticity regulates compartmentalization of synapses. *Nat. Neurosci.* 17:678–685. http://dx.doi.org/10.1038/nn.3682

Ueda, Y., and Y. Hayashi. 2013. PIP_3 regulates spinule formation in dendritic spines during structural long-term potentiation. *J. Neurosci.* 33:11040–11047. http://dx.doi.org/10.1523/JNEUROSCI.3122-12.2013

Vlahos, C.J., W.F. Matter, K.Y. Hui, and R.F. Brown. 1994. A specific inhibitor of phosphatidylinositol 3-kinase, 2-(4-morpholinyl)-8-phenyl-4H-1-benzopyran-4-one (LY294002). *J. Biol. Chem.* 269:5241–5248.

Woods, G., and K. Zito. 2008. Preparation of gene gun bullets and biolistic transfection of neurons in slice culture. *J. Vis. Exp.* 12:e675.

Wu, C.H., C. Fallini, N. Ticozzi, P.J. Keagle, P.C. Sapp, K. Piotrowska, P. Lowe, M. Koppers, D. McKenna-Yasek, D.M. Baron, et al. 2012. Mutations in the profilin 1 gene cause familial amyotrophic lateral sclerosis. *Nature.* 488:499–503. http://dx.doi.org/10.1038/nature11280

Yuste, R., and T. Bonhoeffer. 2001. Morphological changes in dendritic spines associated with long-term synaptic plasticity. *Annu. Rev. Neurosci.* 24:1071–1089. http://dx.doi.org/10.1146/annurev.neuro.24.1.1071